

Thermo-mechanical design and testing of a microbalance for space applications

Diego Scaccabarozzi^{a,*}, Bortolino Saggin^a, Marco Tarabini^a, Ernesto Palomba^b,
Andrea Longobardo^b, Emiliano Zampetti^c

^a Politecnico di Milano, Polo Territoriale di Lecco, Via G. Previati 1c, 23900 Lecco, Italy

^b IAPS-INAf– Istituto di Astrofisica e Planetologia Spaziali, via del Fosso del Cavaliere 100, 00133 Roma, Italy

^c CNR-Istituto sull'Inquinamento Atmosferico, via Salaria Km 29,300, 00015 Monterotondo, Roma, Italy

1. Introduction

Some phenomena in the solar system can be analyzed only through in situ measurements. Typical examples are the study of the dynamics and physical characteristics of space environment powders released by cometary nuclei (Colangeli et al., 2007) or present in planets' atmospheres and in planetary orbit environment (Srama et al., 2011). Combination of quartz crystal microbalance (QCM) and

thermogravimetric analysis (TGA) has been also exploited for contamination testing in space (McKeown, 1998; Sekler and Wobmann, 2003; Wood et al., 1997) or to measure in situ mass deposition as a function of temperature and time (Battaglia et al., 2004; Palomba et al., 2002; Zinzi et al., 2011). The TGA is used to characterize materials that exhibit weight loss or gain due to kinetic processes, i.e. decomposition, oxidation or dehydration. Once a material sample is heated, its most volatile components desorb or sublimate and its mass can be obtained as mass difference between before and after desorption. Moreover, chemical composition of the desorbed component can be inferred

* Corresponding author.

E-mail address: diego.scaccabarozzi@polimi.it (D. Scaccabarozzi).

from its desorption temperature, as well as by measuring its enthalpy of sublimation (Albyn, 2001).

Any change of sample mass causes QCM resonance variation that can be determined through the Sauerbrey relation (Sauerbrey, 1959):

$$\Delta f = -\Delta M \frac{2f_0^2}{A\sqrt{G\rho_q}}, \quad (1)$$

where Δf is measured resonance shift, ΔM is the deposited mass change and f_0 is the unloaded crystal resonance frequency. A , G and ρ_q are parameters describing the microbalance, respectively the electrode area and the quartz torsional modulus and density. On the basis of Eq. (1), QCM first shear resonance linearly changes with the deposited mass. Linear behavior is assured up to 2% mass loading (Benes, 1984) since beyond that range, the relation becomes nonlinear (Lu, 1974). Prediction of the maximum mass loading accommodated by QCM before nonlinearity is difficult to assess, because it depends on many factors such as the quality of the quartz crystal, the acoustic losses in the coated material, the stresses generated in the crystal by deposited material and the design of the crystal holder and oscillator circuitry (Reed et al., 1990).

The VISTA instrument is based on lightweight piezoelectric crystal microbalances. Different versions of the instrument have been developed for many planetary in situ missions. VISTA has been studied for sample return missions from primitive asteroids (e.g. Marco Polo and MarcoPolo-R missions) and is currently part of the MarcoPolo-R scientific payload, where it aims to monitor the dust raised by the sampling operations and to measure the water and organics content of the asteroidal regolith (Palomba et al., 2013). Moreover, VISTA has been studied for in situ measurements on the Jupiter icy satellites (Europa and Ganymede), to detect organic molecules, discriminate water ice and clathrate hydrates and infer the composition of non-ice materials (Gowen et al., 2011).

A lightweight QCM has been also developed for DREAMS, the scientific package mounted on the Entry and Descent Module of the ExoMars 2016 mission (Palomba et al., 2011). In this scenario, VISTA aims to measure the dust mass loading on Mars, water ice fall at low latitudes and physically adsorbed water content in the Martian dust. In all the cited VISTA versions, the microbalance is equipped with a built-in heater system allowing to perform micro TGA measurements of fine grained particles of less than 10 μm size. A mockup of the sensing element has been manufactured and successfully tested (Zinzi et al., 2011) validating the feasibility of the proposed concept about the intended desorption studies. The development of the instrument up to a flight model requires coping with the expected mechanical and thermal environments during launch and landing. For the design phase, an equivalent quasi-static acceleration level of 1000 m/s^2 has been used to account for the excitation levels expected at the instrument landing (Saggini et al., 2007,

2011; Scaccabarozzi et al., 2014). Moreover, high temperature gradients are expected on the microbalance, given that the crystal temperature varies between -100°C during accumulation phases and 400°C during the thermo-gravimetric analyses. The higher value limits usage of SiO_2 microbalance crystals since phase transition phenomenon for quartz starts at approximately 570°C (Webster, 1999) but its piezoelectric properties begin to worsen at lower temperatures. Anyway, the use of gallium orthophosphate as material substrate (as in the MarcoPolo-R version of VISTA) allows achieving working temperatures close to 900°C , providing also an higher piezoelectric sensitivity (Aizawa et al., 2006; Elam and Pellin, 2005; Jakab et al., 2009; Krispel et al., 2003).

In this work, we focus on the thermo-mechanical design and testing of the VISTA QCM developed for the Martian application, but many of the result of the performed analysis can be transferred to other in situ monitoring, like the one required on asteroids or spacecrafts, where the environment is less demanding.

The next section presents the thermo-mechanical design of the crystal microbalance holding system. Section 3 describes the design and optimization of the micro-heater, implemented on quartz crystal microbalance. Tests in the expected mechanical environment and validation of the thermal control are summarized in Sections 4 and 5. Paper conclusions are drawn in Section 6.

2. Thermo-mechanical design

2.1. The holding concept

The microbalance and the support scheme are shown in Fig. 1. The mechanical holding system is made of two groups of elastic elements, as shown on the right part of Fig. 1. Elements A constraint the crystal to the housing, warrant mechanical resistance against the expected dynamic loads and ensure a proper thermal insulation of the quartz crystal. Elements B grant a stable contact between the crystal and the A elements by an appropriate load; both A and B elements act as electric contacts, allowing heater control and measurement of the crystal natural frequency and temperature.

The necessity of using a mechanical contact instead of a soldered one arises from the request of reliability in the vibrational environment and from the wide temperature working range. The small thickness of the conductive material deposited on the crystal and its adhesion have proved to be critical at the soldering pads, mostly in case of thermal cycling. Thus, the holding system design required accomplishing different tasks:

- Elements A had to be designed to provide resistance against static and dynamic loads and to avoid the thermo-elastic stresses on the brittle crystal.
- Elements B had to be designed to avoid the crystal sliding in case of transverse loading and to assure a reliable and stable electrical contact in the harsh

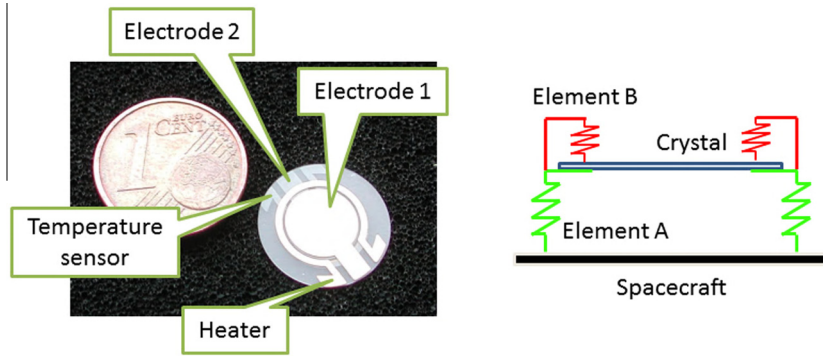


Fig. 1. Left: mockup of VISTA instrument. Right: schematic of the microbalance holding system.

thermo-mechanical environment (large temperature differences are generated during thermo-gravimetric analysis).

2.2. Thermo-mechanical design constraints

The microbalance has been designed in order to withstand:

- Quasi-static acceleration of 1000 m/s^2 representing the shock at landing on Mars (well higher than the shock at landing on an asteroid).
- Sine excitation with amplitude 200 m/s^2 in the frequency range from 20 to 60 Hz.
- Random excitation in the frequency band from 20 to 2000 Hz with an RMS of 500 m/s^2 .

The thermal environment foresees at the mounting interface a temperature between -100 and $30 \text{ }^\circ\text{C}$ (or up to $110 \text{ }^\circ\text{C}$ in the case of a Near-Earth asteroid) and the convective environment due to the Martian atmosphere in the same range, with maximum wind speed of 25 m/s (high vacuum in case of asteroid environment). Whatever the mission scenario, large temperature differences with respect to the environment are to be achieved because the crystal must be heated up to $400 \text{ }^\circ\text{C}$ during thermo-gravimetric analyses.

2.3. Elements A design

The microbalance is supported by three C-shaped titanium alloy beams (Ti-6Al-4V) positioned symmetrically at 120° . The mounting height is 13 mm , in order to reduce the assembly size but allowing for the volume required by the proximity electronics. The symmetric three-blade configuration provides an iso-static mounting, a recurrent requirement in the design of space-devoted instruments (Saggin et al., 2010) to reduce the thermo-elastic stresses that would derive from the extreme environmental temperature ranges. Among the various advantages of this titanium alloy, the high resistance/density ratio and low

coefficient of thermal expansion are the most relevant for our application.

Since the acceleration direction during landing is unknown, the equivalent quasi-static load has been applied along three mutually perpendicular directions. The reference system shown in Fig. 2 identifies two orthogonal directions in the microbalance plane, hereafter named X and Y , and one perpendicular to the sensor area (Z). When the acceleration acts along Z , buckling is expected to be the most critical condition for the supporting structure whereas in case of in-plane loading, the bending stresses are the most relevant. Thus, the mechanical design of elements A was driven by the following requirements:

- Resistance against eccentric compressional load (buckling condition).
- Limited deflection under the acceleration loads.
- First natural frequency of the assembly larger than 150 Hz .
- Thermo-elastic stresses below the safety limit.

Since the crystal thickness (0.16 mm) is limited in comparison to its diameter (14 mm), any bending torque must be avoided. A preliminary design based on analytical approach was performed in order to identify the minimum/maximum allowed thickness that satisfies the requirements in each condition. Then, the design was verified with a Finite Elements (FE) model. Table 1 summarizes the design limits of the support thickness for all the conditions

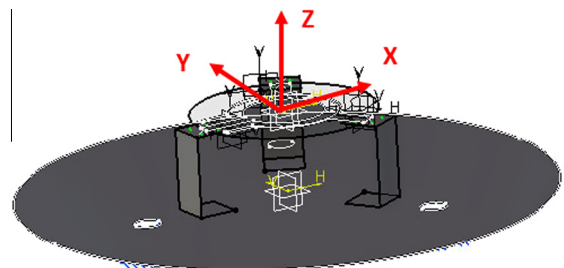


Fig. 2. FE Mechanical model of the microbalance with the reference system.

Table 1
Summary of the limit support thicknesses.

Condition	Thickness [mm]
Buckling	0.01
Bending Torque	6.1×10^{-5}
Support dynamic behavior	0.02
Thermo-elastic stress	0.6 (max value)

analyzed. The supports thickness was finally set to 0.1 mm; the value satisfies all design requirements and eases the manufacturing process. The microbalance FE model is shown in Fig. 2. Mechanical and thermal properties of the materials used in the modeling are presented in Table 2.

The model shows a large circular base fixed on three points aiming to represent the constraint with the spacecraft interface. The material used for the base is the same of the three supports, i.e. titanium alloy. As crystal material, quartz was used instead of GaPO₄ as worst case due to a lower thermal conductivity and thermal expansion coefficient. The quartz crystal and the supports are rigidly connected at the interface. The supports were modeled with shell elements.

Figs. 3 and 4 show the results of the FE mechanical analyses. In accordance to the ECSS standards, margin of safety (MS) was computed for each condition as

$$MS = \frac{\sigma_{ADM}}{FOS\sigma_{MAX}} - 1, \quad (2)$$

σ_{MAX} and σ_{ADM} are respectively the maximum Von Mises stress and the yield/ultimate stress and FOS is a safety factor against the analyzed condition. The required FOS was 1.5. Computed MSs for the titanium blades are summarized in Table 3. The results validated the supports

Table 2
Mechanical and thermal properties of the materials adopted in the FE models.

Material property	Unit	Ti-6Al-4V	Quartz
Density	kg/m ³	4429	2200
Young's modulus	MPa	110316	71700
Poisson's coefficient		0.31	0.17
Ultimate strength	MPa	924	48
Yield Strength	MPa	869	Not defined
Thermal expansion coefficient	m/(m °C)	8.9×10^{-6}	5.70×10^{-7}
Thermal conductivity	W/(m K)	7.3	1.4

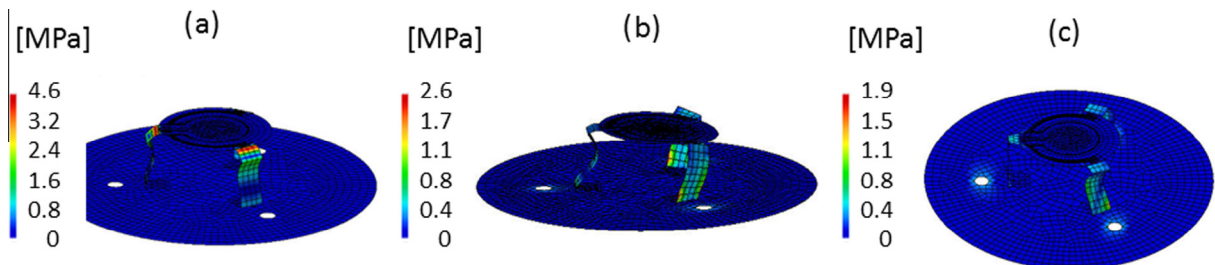


Fig. 3. Von Mises stresses with quasi-static loading. (a) Z axis, (b) X axis, (c) Y axis.

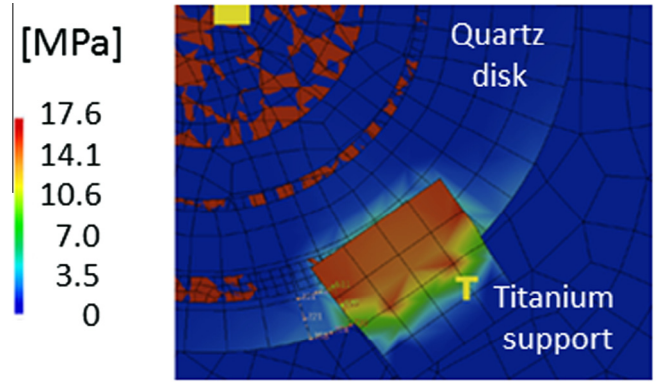


Fig. 4. Zoom of the Von Mises stresses due to thermo-elastic deformation with cooling down to -100 °C in the model region characterized by the highest stresses.

design since MS was always positive. In the thermo-elastic analysis, the most critical for the crystal, the maximum Von Mises stress was 7.38 MPa and the MS was 3.3.

An in-plane movement of the crystal due to the bending of the three supports characterizes the first microbalance vibration mode at a frequency of 1243 Hz.

2.4. Elements B design

Elastic elements are positioned above the microbalance supports in order to secure the quartz, warranting the contact with the three supporting legs in any environmental condition characterizing the whole mission. Moreover, these elements were conceived to provide a reliable electrical contact during the thermogravimetric analyses. Thus, element B design was guided by two requirements:

- The generation of a force sufficient to avoid microbalance slipping for in-plane loadings.
- The creation of a good electrical contact resistance (ECR) in the whole temperature range of interest.

Both conditions were satisfied by properly designing the element B stiffness. The required force to hold the microbalance crystal was determined starting from the support and quartz masses and the friction coefficient of the materials in contact. In accordance with the ECSS standards for the frictional forces in mechanism design, the required resistant force had to be multiplied by a safety factor 3. A scheme of

Table 3
Margins of safety computed from the performed FE analyses.

Condition	σ_{MAX} [MPa]	MS
Z quasi-static loading	4.6	124
X quasi-static loading	2.6	221
Y quasi-static loading	1.95	296
Thermal loading	17.6	32

the mechanical and electric contact is shown in Fig. 5. The titanium alloy blade provides the required stiffness and acts as an electrical connection to the microbalance anode. Cathode connection consists of a metallic film wrapped around a cylinder of insulating material mechanically connected to the anode. The adopted insulator is MACOR[®], a ceramic material suitable for vacuum and high temperature applications. The cylinder radius was evaluated with the Hertz's cylinder-plane contact theory. Minimum radius was 2 mm with a cylinder length of 3 mm.

The stiffness of the elastic element, derived from FE analyses, was chosen to achieve minimum load to cope with the in-plane loading assuming a deformation of 1 mm. Fig. 5 shows the displacement of the element B under 1 N loading.

The ECR of a rectangular constriction (Braunovic et al., 2010) can be expressed as:

$$ECR = \frac{0.86}{\sqrt{A}} \rho, \quad (3)$$

where ρ is the titanium resistivity ($4.2 \times 10^{-7} \Omega m$) and A is the contact area. The latter is function of the contact force, geometry and materials according to the Hertz's contact theory. ECR variation with temperature is related to the change of the contact force caused by the different elongation between the titanium alloy and the quartz crystal in temperature. The thermal properties of the element B materials are listed in Table 2 whereas for the MACOR[®] material, coefficient of thermal expansion is about $9.36 \times 10^{-6} m/(m \text{ } ^\circ C)$. Fig. 6 shows computed ECR between 20 and 450 °C.

The average value is approximately 8.32 mΩ and changes less than 0.1% within the investigated temperature range. Thus, the ECR due to the mechanical contacts is not critical in comparison with the electrical resistance of the heater (that by design is at least four orders of magnitude larger) and/or of the microbalance electrodes.

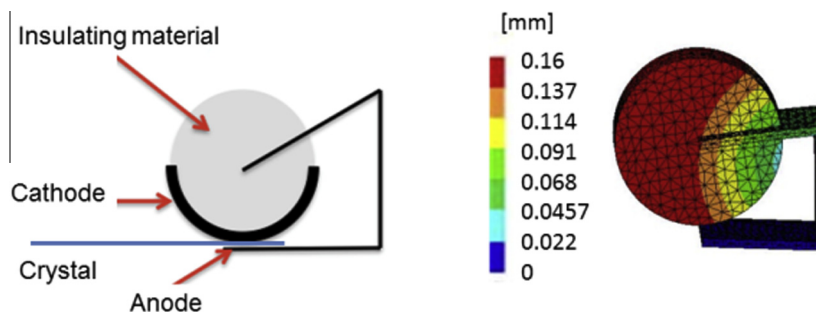


Fig. 5. Left: scheme of the element B geometry. Right: element B displacement under 1 N loading. Maximum displacement is about 0.16 mm.

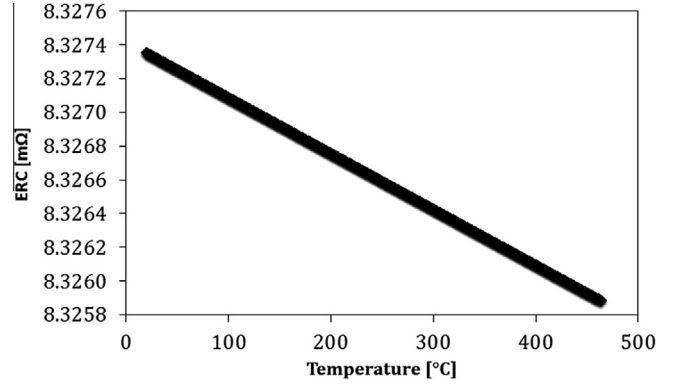


Fig. 6. ECR vs temperature.

2.5. Optimization of the microbalance mounting

The model of the holding system is shown in Fig. 7. The cylindrical insulating parts have been cut in order to reduce the overall mass and elements B (above the microbalance) are directly connected to the A supports. Final geometries of elements A and B are summarized in Table 4. The instrument mass can be additionally reduced by positioning the heater electrical contacts at 120° and superimposing the contacts of the microbalance electrodes as shown in Fig. 7; this improves also the temperature uniformity on the crystal as shown in the next section. The same modification has to be applied to the thermometer contacts on the opposite surface, not shown in Fig. 7.

3. Microbalance heater optimization

3.1. The thermal environment

Different layouts of micro-integrated heaters are reported in literature for a wide range of applications (Macagnano et al., 2009; Sakai et al., 2013). In the intended application, the heater shape was designed to achieve a maximum temperature of 400 °C on the electrode area and at the same time, to minimize the temperature differences over the sensor area. Martian day cycle is characterized by atmospheric temperatures ranging between -120 and 20 °C for equatorial regions in clean sky conditions. For the thermal design it was assumed that the microbalance was operated in a cold

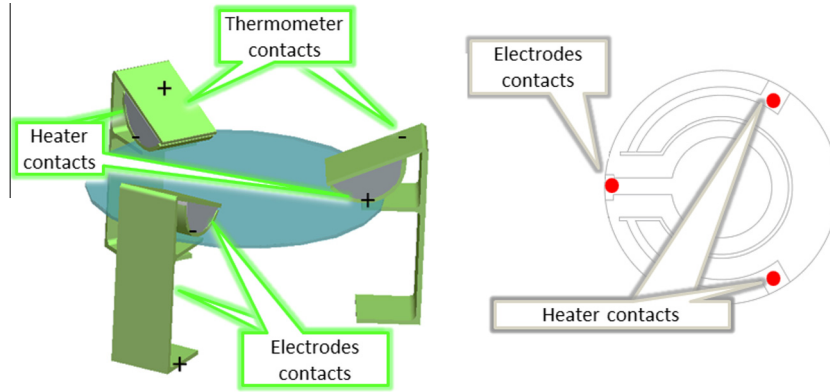


Fig. 7. Left: microbalance holding system. Right: modified film heater/thermometer pattern.

Table 4
Summary of the holding system size.

Dimension	Element A	Element B
Width [mm]	3	2
Height [mm]	9	3
Thickness [mm]	0.1	0.2

environment at $-100\text{ }^{\circ}\text{C}$; this is a worst case because the TGA can be performed during the day.

The thermal design was performed with PTC Pro/MECHANICA thermal analysis tool. An equivalent surface specific conductance of $23\text{ W}/(\text{m}^2\text{ }^{\circ}\text{C})$ was evaluated by linearization of the heat exchange due to radiation with the cold environment. Moreover, the convection coefficient generated by Martian wind varies between 0.25 and $19\text{ W}/(\text{m}^2\text{ }^{\circ}\text{C})$. Thus, in order to simulate the Martian worst case condition (more challenging than the asteroidal worst case condition), a global exchange coefficient of $42\text{ W}/(\text{m}^2\text{ }^{\circ}\text{C})$ was applied over the microbalance surfaces in addition to a temperature constraint of $-100\text{ }^{\circ}\text{C}$ at the supports/spacecraft interface.

3.2. FE modeling and heater optimization

The thermal model includes the three titanium alloy supports and the quartz crystal. Heat flux is directly applied on a region of the crystal that identifies the heater shape. The shape, the heat flux density and its distribution were the design parameters. Fig. 8 shows the heater shape evolution during the design. Table 5 summarizes the heater power and the temperature difference over the electrode area for each condition.

In the starting model, shown in Fig. 8a, the heater radius was 5 mm. When a power of 2 W was supplied to the heater, the desired temperature of $400\text{ }^{\circ}\text{C}$ was reached only in few zones and the maximum temperature difference on the electrode area was of about $150\text{ }^{\circ}\text{C}$. This result highlighted the need of increasing the heating power and changing heater geometry.

Thus, as shown by configuration b, the heater radius was reduced to 4 mm and the heat flow rate was increased

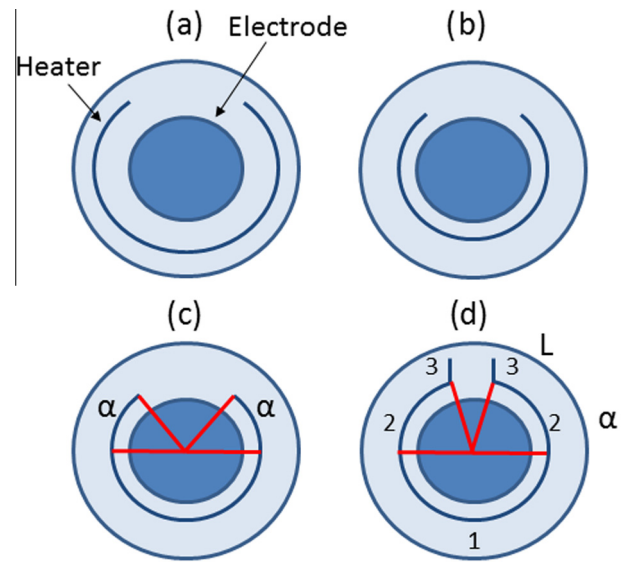


Fig. 8. Evolution of the heater geometry. (a) Heater initial shape. (b) Heater with reduced size (c) different power distribution over the heater circumference. (d) Final heater geometry. Different heater regions are labeled with numbers from 1 to 3.

Table 5
Heater shape optimization results.

Configuration	Heater power [W]	Temperature difference [$^{\circ}\text{C}$]
a	2	150
b	2.5	50
c	3.4	35
d	3.62	20

up to 2.5 W. As result, the radial temperature difference was reduced to $50\text{ }^{\circ}\text{C}$, but it was not possible to enhance further the temperature uniformity. This is due to the asymmetry of the heater shape that cannot be a closed circle because it cannot overlap the electrode pad; a non-uniform distribution of the heat flow rate must be used.

The heat flow rate has been distributed imposing three different heat flux densities to heater regions with variable size. This new configuration is shown in Fig. 8c. The maximum temperature difference within the electrode area

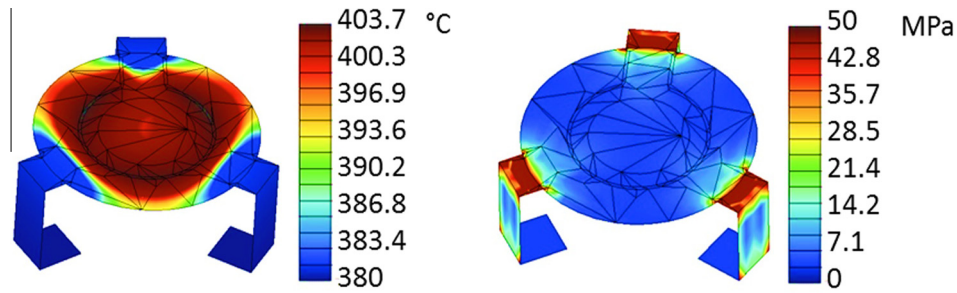


Fig. 9. Left: temperature distribution over the quartz microbalance with the optimized heater shape. Right: Von Mises stresses in the thermo-elastic analysis.

has been minimized by changing the angle α . In this configuration it was found that the upper areas of the heater were both delivering 0.7 W whereas the remaining region was providing 2 W. The desired temperature of 400 °C was reached everywhere inside the central area and the maximum difference of temperature was 35 °C. Moreover, analyzing the temperature distribution it was noticed that the highest power loss is in correspondence of the area where the heater is absent.

Thus, the heater was then extended as shown in Fig. 8d to surround the electrode pad and to reduce as much as possible the region where power delivery is absent. In that configuration, the optimization tool modified both α and L , length of the additional areas. The overall power was eventually 3.6 W distributed as 0.7 W on the upper circular areas (regions number 2 of Fig. 8d), 2 W on the bottom circular part (region number 1) and 0.11 W along the rectangular regions (number 3). The final heater geometry resulted in α and L 60° and 2.4 mm, respectively. As shown in Fig. 9 the average temperature in the central heater area is close to 400 °C and the computed temperature difference is less than 20 °C. This is a noticeable result considering the low thermal conductivity of quartz combined with the constraints on the heater layout.

Stress conditions deriving from the temperature gradients (concentrated on small areas close to the supports) and the support clamps have been evaluated. The thermo-elastic analysis evidenced high stresses in correspondence of the three junctions between the quartz and the supports. These are due to the CTE difference between titanium and quartz rigidly connected at their interface whereas in the real mounting a relative sliding between the supports and quartz is allowed. The maximum stress on the quartz crystal is anyway about 3.6 MPa still by far acceptable being the corresponding MS of about 7.8.

4. Mechanical testing

4.1. Setup description and testing procedure

A mockup of the holding structure, shown in Fig. 10, has been manufactured in order to validate the proposed concept in the expected mechanical environment. The

stainless steel supports were mounted on an aluminum base connected to an electrodynamic shaker. A blank crystal has been used instead of the one with the deposited electrodes.

Two accelerometers were mounted at the shaker interface to measure the feedback control of the shaker (reference accelerometer) and the input acceleration (measurement accelerometer). The acceleration of the crystal was measured by a Polytec vibrometer OFV-500 whose spot was focused on the disk, during vertical vibration, or on the supports for the in-plane excitations. Both accelerometers were fed and amplified by a Bruel & Kjaer Nexus[®] conditioning unit.

The qualification test procedure consisted of the following steps:

- Initial resonance search: a low amplitude sweep sine test between 20 and 2000 Hz, with an acceleration amplitude of 5 m/s² and a sweep rate of 2 oct/min, aiming to identify the main modes and relative amplification factors.
- Sine test: sweep sine excitation with amplitude of 200 m/s² between 20 and 60 Hz.
- Intermediate resonance search: low amplitude sweep sine test with the same parameters of the initial resonance search.
- Random test: random excitation from 20 to 2000 Hz with an equivalent RMS of 500 m/s² for a total time of 2.5 min.
- Final resonance search: low amplitude sweep sine test.
- Microbalance dismounting: the mockup was dismounted and the glass disk was visually inspected.

The testing procedure was applied along X , Y and Z axes.

4.2. FRF results

In order to verify that no damages occurred as a consequence of the high acceleration tests, FRFs (Frequency Response Functions) of each resonance search test were compared. The FRF have been evaluated as the ratio

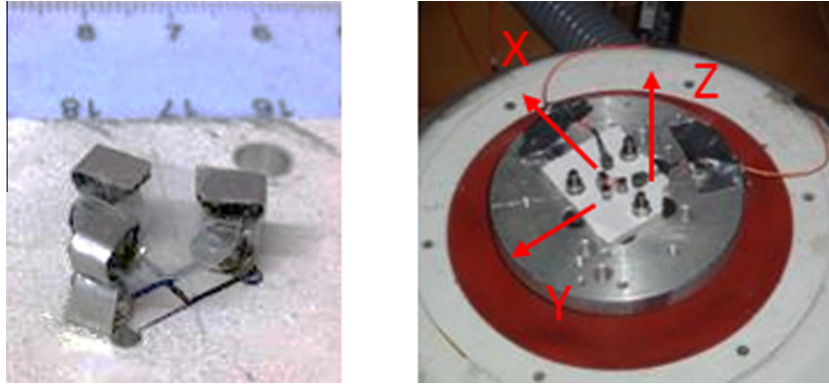


Fig. 10. Left: mockup of the holding supports for the mechanical testing. Right: mockup mounting on the shaker interface and testing reference axes.

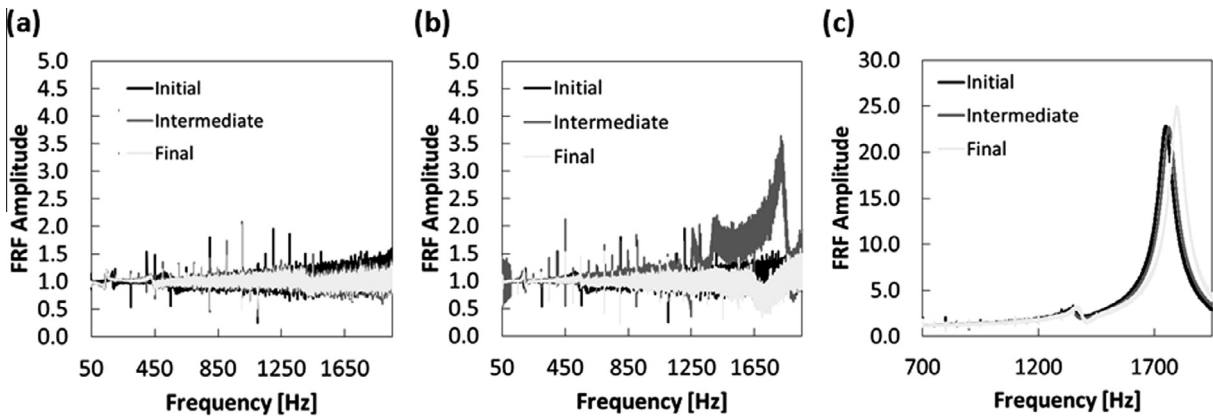


Fig. 11. Comparison between measured FRFs in resonance search testing for each direction. (a) FRFs along X axis. (b) FRFs along Y axis. (c) FRFs along Z axis.

between the spectrum of the microbalance acceleration and the input excitation one. Fig. 11 shows the measured FRFs at initial, intermediate and final resonance search tests for each excitation direction.

No resonances were detected along X and Y directions, being the FRFs amplitude nearly unitary, as shown in Fig. 11a. This result was expected since the only microbalance mode in the band of excitation has a dominant Z component (crystal bending mode) whereas the excitations are in the X - Y plane. Fig. 11b shows FRF amplification compatible with the crystal resonance at 1770 Hz. The small amplification during that test is justified by the laser spot positioning, less carefully centred in the crystal plane, which picked-up the constraint rotation induced by the crystal bending. Microbalance resonance is instead clearly shown in Fig. 12c where the FRFs amplification is 23 at 1770 Hz. The small differences in the natural frequencies from beginning to end of the test ($<1.6\%$) indicates stability of the crystal constraining. The difference between computed and measured resonances (4.6%) validated the FE models. A visual inspection during the testing and at microbalance dismounting did not evidence any damage on the crystal.

5. Thermal testing

5.1. Setup description and testing procedure

The microbalance mock-up was tested in air and vacuum conditions to verify the thermal control system performances. Tests were performed on the original crystal heater geometry, given that the optimized one was not available yet.

The electrical contacts were manufactured with stainless steel foils 0.2 mm thick reproducing the configuration of Fig. 5, two elements were used to feed the heater whereas additional two to connect the microbalance electrodes. Three supports, implementing the same iso-static mounting described above, were realized to hold the microbalance nevertheless, differently from the final design they had no electrical function. The microbalance mockup is shown in Fig. 12.

The testing objectives were:

- Calibration of the microbalance heater (in a controlled temperature bath).

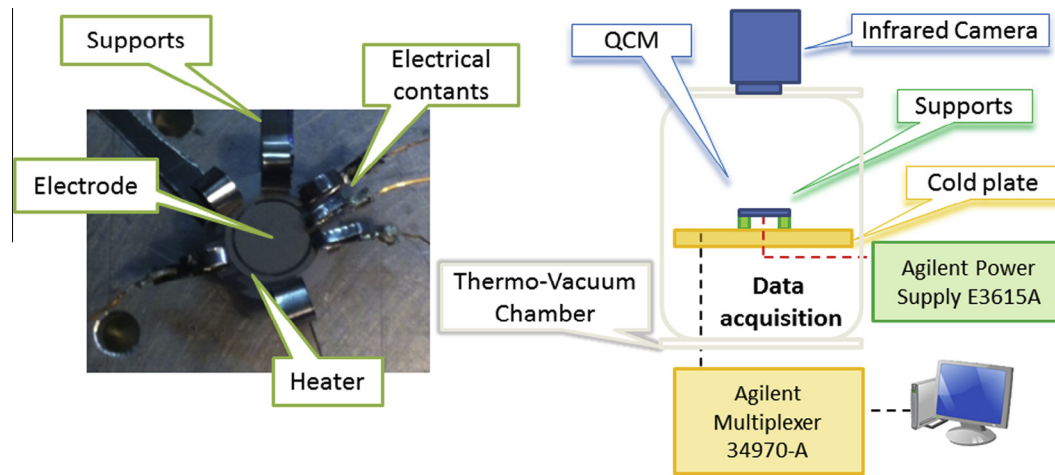


Fig. 12. Microbalance tests in thermo-vacuum conditions. Right: microbalance mockup and mechanical contacts. Left: scheme of the experimental setup.

- Verification of the electrical contacts resistance stability at different temperatures; and
- Measurement of the achieved temperature difference within the electrode area (in air and vacuum conditions).

During vacuum testing, the temperature of the base plate was maintained at 20 °C and the microbalance power supply was varied from 0.13 to 0.56 W in 5 steps. The temperature difference on the electrode area was measured with a NEC TH7102WX infrared camera. This allowed measuring the electrode area temperature without the loading effect that any contact sensor would have on the low thermal conductivity crystal. Moreover, thanks to the spatial resolution of the IR camera, the temperature distribution over the electrode area was measured as well. The microbalance heater was supplied by an Agilent E3615A unit and the pressure inside the chamber was measured by a Varian Pirani-Capacitance Diaphragm gauge PCG-750, with 5×10^{-3} – 1.5×10^5 Pa measuring range. During vacuum testing, the pressure inside the chamber was kept constant at 10^{-3} mbar. The interface temperature, heater resistance and testing pressure were acquired by an Agilent 34970A system. A scheme of the air/vacuum testing setup is shown in Fig. 12. Before the temperature measurement, IR camera was used to assess the emissivity of the electrodes. Deposited titanium emissivity at 60 °C was 0.5 with 12% standard uncertainty. An example of the recorded thermal image is provided in Fig. 13.

Temperature data were analyzed on a square area (10×10 pixels in size) located at the electrode centre. Fig. 13 shows that the microbalance temperature is higher near the heater where there is only one mechanical support (lower thermal dissipation) and decreases at the location of the two mechanical supports and the electrical contacts. This result confirms that the symmetrical configuration of the final design (three mechanical supports/electrical connections placed at 120°) is the best to maximize temperature uniformity on the measurement area.

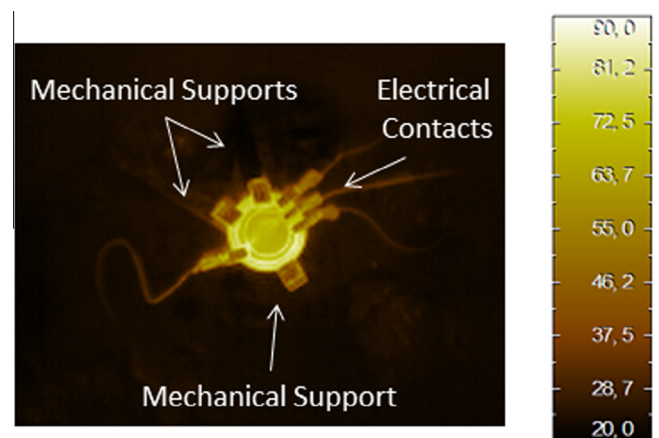


Fig. 13. Thermal image taken by the IR camera. Electrode temperature is about 76 °C with black body emissivity.

5.2. Heater characterization

Two heating and cooling cycles from 20 to 100 °C were performed in a thermal bath in order to measure dependence of the electrical resistance from temperature.

Results (Fig. 14) show a noticeable drift for both the heating/cooling cycles that has been associated with the oxidation of the heater by the fluid (55% ethylene glycol and 45% water). In the first cycle, the drift between heating and cooling is more evident since the resistance was kept at high temperature for a longer time and so a larger more relevant of titanium oxidation occurred. Moreover, the variation of the electrical resistance of the heater is almost linear with the temperature, except for the temperatures above 80 °C. The equivalent sensitivity ($-0.96 \Omega/^\circ\text{C}$ with a standard uncertainty of 2.1%) was identified with a linear regression. The measured resistance is approximately 4.5 k Ω ; this is larger than the design value because the thickness of deposited material (about 0.15 μm by design) of the mock-up was likely lower than the expected one. The high electrical resistance limited the maximum

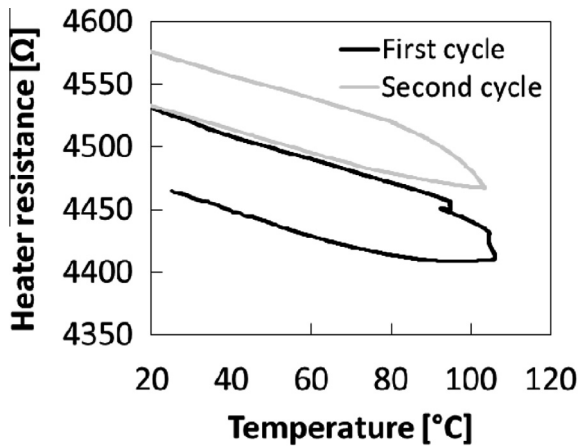


Fig. 14. Heater resistance vs temperature.

achievable temperature at about 100 °C since the maximum allowed supply voltage was 50 V in order to avoid electrical discharges. Moreover, monitoring the heater resistance during microbalance testing allowed measuring also the average electrode area temperature.

Fig. 15 shows the resistance vs. power and power vs. temperature plots computed with the heater sensitivity measured by the IR camera during in air testing. Measured temperature and uncertainties are summarized in Table 6. T_M and T_C in Table 6 are the temperatures measured with the IR camera and derived from heater resistance monitoring, respectively.

Fig. 16 shows the resistance vs. power and power vs. temperature plots computed using the heater sensitivity determined above along with those measured by the IR camera in vacuum conditions. Measured temperature and uncertainties are summarized in Table 7.

5.3. Results and discussion

The air testing confirmed the heater oxidization already observed during the heater characterization (see Fig. 14). A

Table 6

Comparison between heater temperatures measured by means of the IR camera and the heater resistance, air testing.

Resistance [Ω]	Power [W]	T_M [$^{\circ}\text{C}$]	U_M [$^{\circ}\text{C}$]	T_C [$^{\circ}\text{C}$]	U_C [$^{\circ}\text{C}$]
4379	0.13	45.3	4.2	31.0	0.3
4374	0.19	51.0	4.5	39.7	0.3
4364	0.26	58.3	4.9	50.2	0.4
4347	0.46	77.5	6.2	67.4	0.5
4341	0.56	87.2	6.8	74.2	0.5
4349	0.56	87.8	6.9	87.8	0.6
4360	0.46	78.2	6.3	76.1	0.5
4384	0.22	58.3	5.0	51.0	0.4
4392	0.19	51.7	4.6	43.1	0.4
4398	0.14	44.5	4.2	37.1	0.3

difference between the measured resistances at the highest temperatures was detected from heating to cooling, as shown in Fig. 15a. Moreover, the temperature difference in the worst condition, i.e. at the maximum supplied power, was 15 °C within the sensor area. This result was compared with a thermal simulation carried out in the same heat exchange conditions, i.e. radiation and convection with an environment at ambient temperature. The computed maximum temperature difference was about 12 °C. The two results are compatible considering the uncertainty in the temperature measurement of about 7 °C at the maximum supplied power (see Table 6). Thus, validity of the thermal modeling was confirmed.

In vacuum testing no heater resistance drift was observed: this confirmed that the film oxidation was the cause of the phenomenon observed both in the thermal bath and air tests. The temperatures obtained from heater resistance measurement and those measured by the IR camera in vacuum were compatible, proving that the measurement of the film heater resistance is representative of the electrode area temperature. This result makes this microbalance concept particularly suitable to be applied in an atmosphere-less bodies (such as an asteroids or orbiting spacecrafts), where, thanks to the vacuum, no film oxidation should occur.

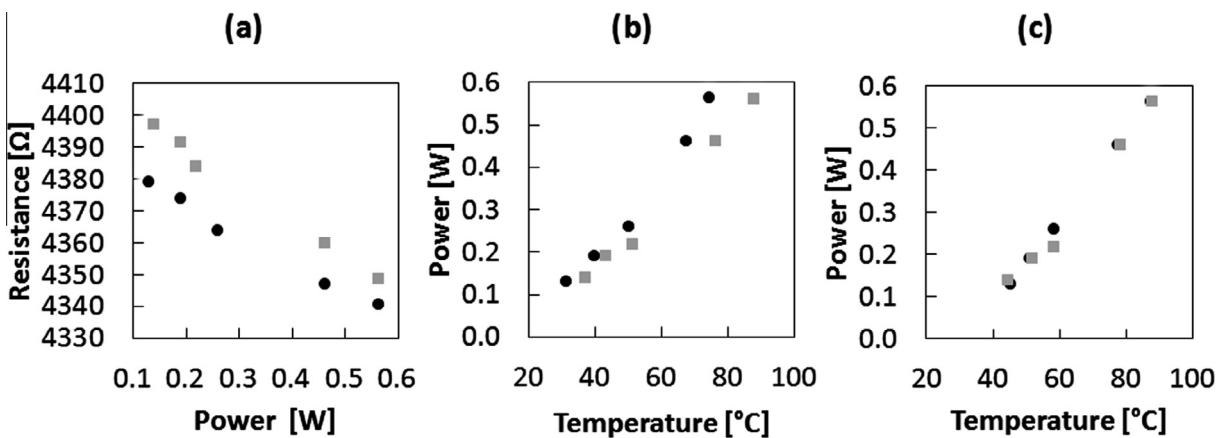


Fig. 15. Air testing results (a) heater resistance vs temperature (b) feeding power vs computed temperature (c) feeding power vs temperature measured with the IR camera. Dots and squares show respectively heating and cooling cycles.

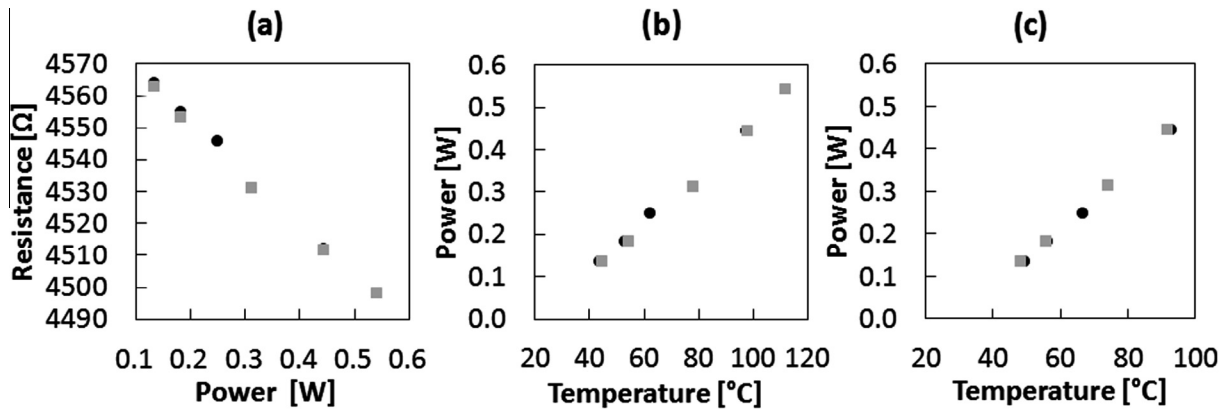


Fig. 16. Hot case testing results (a) heater resistance vs temperature (b) feeding power vs computed temperature (c) feeding power vs temperature measured with the IR camera. Dots and squares show respectively heating and cooling cycles.

Table 7

Comparison between heater temperatures measured by means of the IR camera and the heater resistance, vacuum testing.

Resistance [Ω]	Power [W]	T_M [$^{\circ}\text{C}$]	U_M [$^{\circ}\text{C}$]	T_C [$^{\circ}\text{C}$]	U_C [$^{\circ}\text{C}$]
4564	0.14	49.3	4.3	43.5	0.3
4555	0.18	56.1	4.7	52.8	0.4
4546	0.25	66.4	5.4	62.2	0.4
4512	0.45	92.8	7	97.3	0.6
4498	0.54	102.3	7.7	111.8	0.6
4498	0.54	102.1	7.7	111.8	0.6
4512	0.44	91.8	7	97.9	0.6
4531	0.31	74.2	5.8	77.6	0.5
4554	0.18	55.5	4.7	54.3	0.4
4563	0.14	48.0	4.3	44.5	0.3

6. Conclusions

This work presented the thermal and mechanical design of a microbalance devoted to the in situ analysis of planetary environments. The design led to an optimal configuration where the microbalance is supported by three symmetrical blades made of titanium alloy, which ensures microbalance functionality and integrity in all the expected thermal and mechanical environments. The supporting elements have been designed by means of finite element analyses to withstand an equivalent quasi-static load of 1000 m/s^2 and achieve a lower natural frequency larger than 150 Hz. The proposed mounting structure also includes the electrical connections for the microbalance electrodes, for a heater and for a built in thermometer. The microbalance heater shape was optimized to reach a temperature of $400 \text{ }^{\circ}\text{C}$ with maximum temperature differences within the electrode surface lower than $20 \text{ }^{\circ}\text{C}$.

Environmental mechanical and thermal tests allowed validating the finite element models, although the tests were performed on a microbalance mock-up different from the optimized one. Thermal bath tests evidenced a linear relationship between the heater resistance and the temperature. The experimental activity in air condition evidenced the microbalance heater sensitivity to oxidation,

highlighting the need of investigating a film protection for stable operation in ground conditions. Additional tests are required to fully qualify the microbalance with the optimized heater and mountings up to $400 \text{ }^{\circ}\text{C}$ and verify achievable performances during operation for TGA.

References

- Aizawa, H., Inoue, Y., Yamada, K., Hirata, M., Koyama, M., Kurosawa, S., 2006. Resonant properties of GaPO4 resonator device coated with plasma polymerized styrene film. In: 2006 IEEE International Frequency Control Symposium and Exposition. IEEE, pp. 318–321.
- Albyn, K.C., 2001. Extension of the enthalpy of sublimation for adipic acid to temperatures below $80 \text{ }^{\circ}\text{C}$. *J. Chem. Eng. Data* 46, 1415–1416.
- Battaglia, R., Palomba, E., Palumbo, P., Colangeli, L., Della Corte, V., 2004. Development of a micro-balance system for dust and water vapour detection in the Mars atmosphere. *Adv. Space Res.* 33, 2258–2262.
- Benes, E., 1984. Improved quartz crystal microbalance technique. *J. Appl. Phys.* 56, 608–626.
- Braunovic, M., Myshkin, N.K., Konchits, V.V., 2010. *Electrical Contacts: Fundamentals, Applications and Technology*. CRC Press.
- Colangeli, L., Lopez Moreno, J.J., Palumbo, P., 2007. GIADA: the grain impact analyser and dust accumulator for the rosetta space mission. *Adv. Space Res.* 39, 446–450.
- Elam, J., Pellin, M., 2005. GaPO4 sensors for gravimetric monitoring during atomic layer deposition at high temperatures. *Anal. Chem.* 77, 3531–3535.
- Gowen, R., Smith, A., Fortes, A.D., et al., 2011. Penetrators for in situ subsurface investigations of Europa. *Adv. Space Res.* 48, 725–742.
- Jakab, S., Picart, S.b., Tribollet, B., Rousseau, P., Perrot, H., Gabrielli, C., 2009. Study of the dissolution of thin films of cerium oxide by using a GAPO4 crystal microbalance. *Anal. Chem.* 81, 5139–5145.
- Krispel, F., Reiter, C., Neubig, J., et al., 2003. Properties and applications of singly rotated GaPO4 resonators. In: *Proceedings of the 2003 IEEE International on Frequency Control Symposium and PDA Exhibition Jointly with the 17th European Frequency and Time Forum*. IEEE, pp. 668–673.
- Lu, C., 1974. Mass determination with piezoelectric quartz crystal resonators. *J. Vac. Sci. Technol.* 12, 578–583.
- Macagnano, A., Pantalei, S., Zampetti, E., 2009. Exploitation of a simple integrated heater for advanced QCM sensors. In: *Publishers, N.S., (Ed.), Horizons in World Physics*.
- McKeown, D., 1998. Quartz crystal instrumentation for space research. In: *SPIE's International Symposium on Optical Science, Engineering, and Instrumentation, International Society for Optics and Photonics*, pp. 113–125.

- Palomba, E., Colangeli, E.L., Palumbo, P., Rotundi, A., Perrin, J.M., Bussoletti, E., 2002. Performance of micro-balances for dust flux measurement. *Adv. Space Res.* 29, 1155–1158.
- Palomba, E., Longobardo, A., Zinzi, A., et al., 2011. VISTA for DREAMS-ExoMars 2016. EPSC-DSP Joint Meeting. pp. 87.
- Palomba, E., Longobardo, A., Zinzi, A., et al., 2013. VISTA thermogravimeter device for MarcoPolo-R. EPSC 2013-619.
- Reed, C.E., Kanazawa, K.K., Kaufman, J.H., 1990. Physical description of a viscoelastically loaded AT-cut quartz resonator. *J. Appl. Phys.* 68, 1993–2001.
- Saggin, B., Alberti, E., Comolli, L., Tarabini, M., Bellucci, G., Fonti, S., 2007. MIMA, a miniaturized infrared spectrometer for Mars ground exploration: Part III. Thermomechanical design. Remote Sensing. International Society for Optics and Photonics, pp. 67441S-S-10.
- Saggin, B., Tarabini, M., Scaccabarozzi, D., 2010. Infrared optical element mounting techniques for wide temperature ranges. *Appl. Opt.* 49, 542–548.
- Saggin, B., Scaccabarozzi, D., Tarabini, M., Bellucci, G., 2011. Design and testing of a miniaturized Fourier transform infrared spectrometer for Mars observation. In: 3rd CEAS Conference. Venice.
- Sakai, J., Iida, N., Sohgawa, M., Abe, T., 2013. Design and evaluation of microheater combined QCM array for thermal desorption spectroscopy. In: The 17th International Conference on Solid-State Sensors, Actuators and Microsystems (TRANSDUCERS & EUROSENSORS XXVII), 2013 Transducers & Eurosensors XXVII, IEEE, pp. 234–237.
- Sauerbrey, G., 1959. Use of quartz vibration for weighing thin films on a microbalance. *Z. Phys.* 155, 206–222.
- Scaccabarozzi, D., Saggin, B., Alberti, E., 2014. Design and testing of a roto-translational shutter mechanism for planetary operation. *Acta Astronaut.* 93, 207–216.
- Sekler, J., Wobmann, L., 2003. Development of a European QCM-outgassing detector with miniaturised interfaces. *Mater. Space Environ.*, 515–519.
- Srama, R., Kempf, S., Moragas-Klostermeyer, G., et al., 2011. The cosmic dust analyser onboard cassini: ten years of discoveries. *CEAS Space J.* 2, 3–16.
- Webster, J.-G., 1999. *The Measurement, Instrumentation, and Sensors: Handbook*. Springer.
- Wood, B., Bertrand, W., Hall, D., Lesho, J., Uy, O., Dyer, J., 1997. MSX satellite flight measurements of contaminant deposition on a CQCM and on TQCMs. Arnold engineering development center Arnold AFS, TN.
- Zinzi, A., Palomba, E., Zampetti, E., et al., 2011. Exploring the feasibility of volatile desorption studies by means of a quartz crystal microbalance with an integrated micro-heater. *Sens. Actuators A Phys.* 172, 504–510.